

# Atmospheric Sterile Neutrinos

Takehiko Asaka<sup>\*†</sup> and Atsushi Watanabe<sup>†</sup>

*\*Department of Physics, Niigata University, Niigata 950-2181, Japan*

*†Max-Planck-Institut für Kernphysik, Saupfercheckweg 1, 69117 Heidelberg, Germany*

(February 3, 2012)

## Abstract

We study production of sterile neutrinos in the atmosphere and their detection at Super-Kamiokande. A sterile neutrino in the mass range  $1 \text{ MeV} \lesssim M_N \lesssim 105 \text{ MeV}$  is produced by muon or pion decay, and decays to an electron-positron pair and an active neutrino. Such a decay of the sterile neutrino leaves two electron-like Cherenkov rings in the detector. We estimate the sterile neutrino flux from the well-established active neutrino fluxes and study the number of the decay events in the detector. The upper bounds for the active-sterile mixings are obtained by comparing the  $2e$ -like events from the sterile neutrino decays and the observed data by Super-Kamiokande. The upper bound for the muon type mixing  $\Theta_\mu$  is found to be  $|\Theta_\mu|^2 \lesssim 5 \times 10^{-5}$  for  $20 \text{ MeV} \lesssim M_N \lesssim 80 \text{ MeV}$ , which is significantly loosened compared to the previous estimation. We demonstrate that the opening angle and the total energy of the rings may serve as diagnostic tools to discover the sterile neutrinos in further data accumulation and future upgraded facilities. The directional asymmetry of the events is a sensitive measure of the diminishment of the sterile neutrino flux due to the decays on the way to the detector.

# 1 Introduction

The existence of nonzero neutrino masses has been confirmed in the last few decades and stimulated the activities aiming for the theory beyond the Standard Model. Among various possible ways to introduce the neutrino masses into the model, adding gauge singlet fermions (right-handed neutrinos) is one of the most economical and attractive methods. In particular, the seesaw mechanism [1] naturally accounts for the observation that the neutrino masses are very small compared to the other fermions. Moreover, it also gives a natural prescription for the baryon asymmetry of the universe by the leptogenesis scenario [2].

Besides the usual higher mass scales of the right-handed neutrinos around the grand unification scale, the lower mass ranges are also interesting and rich in phenomenology. For example, a keV sterile neutrino is a viable dark matter candidate [3, 4] and accounts for the pulsar velocities [5] due to feebleness of its interactions. Two quasi-degenerate sterile neutrinos in the mass range  $\mathcal{O}(10^{-1}) - \mathcal{O}(10)$  GeV provide viable baryogenesis scenario alternative to the leptogenesis [6, 7, 8]. Remarkably, these excellent features originate in a single framework so called  $\nu$ MSM [4, 7], which is an extension of the Standard Model with three generations of the right-handed neutrinos. Due to lower threshold energies of the production, such “light” sterile neutrinos are more likely to be tested in existing and forthcoming experiments than the usual right-handed neutrinos with super heavy masses (for example, see Ref. [9] and references therein). Mass range by mass range, the sterile neutrinos may provide unique signals in various circumstances. It is thus interesting to study how to produce and detect the sterile neutrinos.

In this paper, we focus on the sterile neutrinos with the mass range  $1 \text{ MeV} \lesssim M_N \lesssim 105 \text{ MeV}$  and study their production in the atmosphere. The previous neutrino experiments, including peak searches in the meson decays [10, 11, 12, 13, 14] and the decay search with accelerators [15, 16], have placed certain bounds on the active–sterile mixing matrix in this mass range. The atmospheric sterile neutrino provides an independent and complementary test to these experiments with artificial neutrino sources. In particular, the peak searches of the pion and kaon decays put no stringent bound on the muon type mixing angle around  $M_N = 40 \text{ MeV}$ . This spot will be effectively probed by the atmospheric sterile neutrino since the sterile neutrinos in this mass range can be copiously produced by the muon decays similar to the atmospheric active neutrinos.

The production of sterile neutrinos in the atmosphere and their detection at Super-

Kamiokande (SK) has been discussed in Ref. [17]. In this work, we extend and improve their work in both sterile neutrino production and its detection. In the flux estimation, we carefully consider the production of the sterile neutrino not only by the  $\mu^\pm$  decay, but also by the  $\pi^\pm$  decay. The sterile neutrino flux does not receive the  $\pi^\pm$  contributions for  $M_N \gtrsim 35$  MeV when the mixing with electron is sufficiently small (as we will show later, this is indeed the case by considering the bounds on the mixings from direct search experiments), being different from the  $\nu_\mu$  and  $\bar{\nu}_\mu$  fluxes. We also take into account the energy distribution of the daughter (the sterile neutrino) in the parent (mainly muon) decay and the phase space suppression due to the sterile neutrino mass. With the sterile neutrino mass around the neighborhood of the muon mass threshold, the flux gets suppressed and the mixing bounds are significantly loosened compared to Ref. [17]. Furthermore, we study the kinematics of the detection process  $N \rightarrow e^-e^+\nu$  in detail, which include the distributions of the opening angle and the visible energy of the emitted  $e^-$  and  $e^+$ . We estimate the upper bounds on the mixing angles by using 1489 days SK data [18]. In this estimation, we shall apply the cut to the events by requiring the visible energy being larger than 30 MeV in accordance with the SK data. This treatment also changes the previous results.

This paper is organized as follows. In Section 2, we calculate the sterile neutrino fluxes produced in the atmosphere. In Section 3, the sterile neutrino decay  $N \rightarrow e^-e^+\nu$  and its event rate at SK are studied. Section 4 is devoted to conclusions.

## 2 Fluxes of the sterile neutrinos

We consider a gauge-singlet fermion  $N$  with the mass range  $1 \text{ MeV} \lesssim M_N \lesssim 105 \text{ MeV}$  which mixes with the left-handed neutrino  $\nu_\alpha$  ( $\alpha = e, \mu, \tau$ ) as

$$\nu_\alpha = U_{\alpha i} \nu_i + \Theta_\alpha N, \quad (1)$$

where  $U_{\alpha i}$  is the Pontecorvo-Maki-Nakagawa-Sakata (PMNS) matrix,  $\nu_i$  ( $i = 1, 2, 3$ ) are the mass eigenstates of the active neutrinos. The parameter  $\Theta_\alpha$  is the mixing between active and sterile neutrinos, which rules the interaction strength of  $N$ . The extension to the multi-generation case is trivially done by replacing  $\Theta_\alpha N$  with  $\sum_I \Theta_{\alpha I} N_I$ . Throughout this work, we focus on the case where the sterile neutrino  $N$  is mainly mixed with  $\nu_\mu$  for the sake of simplicity. That is, we assume  $|\Theta_\mu| \gg |\Theta_e|, |\Theta_\tau|$ , unless otherwise stated.

Indeed, the electron type mixing  $\Theta_e$  is much more severely constrained than the other two parameters. The peak search with  $\pi^\pm \rightarrow e^\pm N$  mode suggests  $|\Theta_e|^2 \lesssim 10^{-8} - 10^{-7}$  for

40 MeV  $\lesssim M_N \lesssim 140$  MeV, while the decay search with accelerators indicate the upper bound for  $|\Theta_\mu|^2$  varies from  $10^{-4}$  to  $10^{-6}$  in the mass range  $10 \text{ MeV} \lesssim M_N \lesssim 100 \text{ MeV}$  [17]. In the case of  $\Theta_\mu$  dominance, the main decay mode of  $N$  is  $N \rightarrow 3\nu$  and the subdominant mode is  $N \rightarrow e^-e^+\nu_\mu$  conducted by the neutral currents. The decay width of each process is given by

$$\Gamma(N \rightarrow 3\nu) = \frac{G_F^2 M_N^5 |\Theta_\mu|^2}{192\pi^3}, \quad (2)$$

$$\Gamma(N \rightarrow e^-e^+\nu) = \Gamma(N \rightarrow 3\nu) \left( \frac{1}{4} - \sin^2 \theta_W + 2 \sin^4 \theta_W \right). \quad (3)$$

In this paper, we focus on the case where the neutrinos are the Majorana particles. Then the lifetime of the sterile neutrino is given by  $\tau \simeq 1/2\Gamma(N \rightarrow 3\nu) = 1.1 \times 10^{-6} \frac{1}{|\Theta_\mu|^2} \left( \frac{100 \text{ MeV}}{M_N} \right)^5$  (s) and the corresponding decay length is  $\simeq 0.33 \frac{1}{|\Theta_\mu|^2} \left( \frac{100 \text{ MeV}}{M_N} \right)^6$  (km) for  $E_N = 100$  MeV sterile neutrinos. For  $|\Theta_\mu|^2 = 10^{-4}$  and  $M_N = 100$  MeV for example, the decay length is about half of the earth radius  $R_\oplus \approx 6,400$  km. The branching ratio of the detectable mode is  $\simeq 1/4 - \sin^2 \theta_W + 2 \sin^4 \theta_W = 0.13$ .

The sterile neutrinos are produced from charged pions and muons in the same manner as the active neutrinos. The main production processes are

$$\begin{aligned} \pi^\pm &\rightarrow \mu^\pm N, \\ \mu^\pm &\rightarrow e^\pm \nu_e (\bar{\nu}_e) N. \end{aligned}$$

The former channel is open only for  $M_N < m_{\pi^\pm} - m_\mu \approx 35$  MeV. The kaon contribution is negligible in the energy range of present concern. In the muon neutrino production for example,  $K^\pm$  contribution becomes significant only in the high-energy regime  $E_\nu \gtrsim 100$  GeV [19].

In fact, the vital part of the sterile neutrino flux is low-gamma regime  $\gamma \lesssim 10$  for an evaluation of the detectability of the atmospheric sterile neutrinos\*. Namely, we are interested in the sterile neutrino spectrum at most up to 1 GeV for the mass range of  $1 \text{ MeV} \lesssim M_N \lesssim 105 \text{ MeV}$ . As we will discuss in Section 3 in detail, the sterile neutrinos are detected by the decay  $N \rightarrow e^-e^+\nu$  which leaves 2e-like rings in the detector. If the gamma factor of the sterile neutrino is too large, the two fuzzy rings will overlap each other and the separation of the rings becomes difficult. Indeed, it turns out that 50% (80%) of the whole events will be observed with the opening angle less than  $20^\circ$  for  $\gamma = 6$  (10).

---

\*Here and henceforth, we use the symbol  $\gamma$  to denote the gamma factor of the sterile neutrino unless otherwise mentioned.

It is in general a complicated task to calculate the flux for such low-energy regime since it is affected by solar activity and the geomagnetic field. In this work, we do not compute the flux from the primary cosmic ray spectrum directly, but we try to reconstruct a reasonable parent's (muons and pions) spectrum from the well-established active neutrino fluxes available in literature [20, 21] and then evaluate the sterile neutrino flux from the reconstructed parent fluxes.

The procedure goes as follows. We start from the  $\nu_e$  and  $\bar{\nu}_e$  fluxes at SK site [20] to estimate the muon fluxes. The evolution of the neutrino flux  $\phi_{\bar{\nu}_e}(E_\nu, t)$  is described by [19]

$$\frac{d\phi_{\bar{\nu}_e}(E_\nu, t)}{dt} = \int_{E_\nu}^{\infty} dE \frac{\phi_{\mu^-}(E, t)}{\lambda(E, t)} \frac{1}{\Gamma} \frac{d\Gamma}{dE_\nu}(E, E_\nu), \quad (4)$$

where  $t$  is the slant depth,  $\phi_{\mu^-}(E, t)$  is the muon flux,  $E_\nu(E)$  is the neutrino (parent  $\mu^-$ ) energy,  $\lambda = \rho(t)\sqrt{(E/m_\mu)^2 - 1}/\Gamma$  is the muon decay length multiplied by the density of the atmosphere  $\rho(t)$ ,  $\Gamma$  is the decay width for  $\mu^- \rightarrow e^- \bar{\nu}_e \nu_\mu$  in the laboratory frame. By integrating (4) with respect to  $t$ , one finds

$$\phi_{\bar{\nu}_e}(E_\nu, t_f) = \int_{E_\nu}^{\infty} dE \Phi_{\mu^-}(E) \frac{1}{\Gamma} \frac{d\Gamma}{dE_\nu}(E, E_\nu), \quad \Phi_{\mu^-}(E) \equiv \int_0^{t_f} dt \frac{\phi_{\mu^-}(E, t)}{\lambda(E, t)}, \quad (5)$$

where  $t_f$  is the depth corresponding to the sea level. The sterile neutrino flux  $\phi_N(E_N, t)$  obeys the similar equation to the active neutrinos if the sterile neutrino decay in the atmosphere is negligible. In fact, the decay length for  $N \rightarrow 3\nu$  is much larger than the altitude of the mesosphere edge  $\approx 100$  km for most of the parameter space. Only exception is the regime  $|\Theta_\mu|^2 \gtrsim 6.6 \times 10^{-3} \left(\frac{100 \text{ MeV}}{M_N}\right)^6 \left(\frac{E_N}{100 \text{ MeV}}\right)$  where  $N \rightarrow 3\nu$  is so rapid that some of the sterile neutrinos do not reach the detector. This means for example, the following estimation of the sterile neutrino spectrum is not reliable and may get additional suppression for  $E_N \lesssim 100$  MeV in the parameter regime  $|\Theta_\mu|^2 \gtrsim 6.6 \times 10^{-3} \left(\frac{100 \text{ MeV}}{M_N}\right)^6$ . Putting aside this strong interacting regime, we have

$$\phi_N(E_N, t_f) = \int_{E_N}^{\infty} dE \left( \int_0^{t_f} dt \frac{\phi_{\mu^-}(E, t)}{\lambda'(E, t)} \right) \frac{1}{\Gamma'} \frac{d\Gamma'}{dE_N}(E, E_N), \quad (6)$$

where  $\lambda'$  and  $\Gamma'$  are the decay length and width for the mode  $\mu^- \rightarrow e^- \bar{\nu}_e N$ . By using  $\lambda' = (\Gamma/\Gamma')\lambda$ , one finds

$$\phi_N(E_N, t_f) = \frac{\Gamma'}{\Gamma} \int_{E_N}^{\infty} dE \Phi_{\mu^-}(E) \frac{1}{\Gamma'} \frac{d\Gamma'}{dE_N}(E, E_N), \quad (7)$$

$$\frac{\Gamma'}{\Gamma} = |\Theta_\mu|^2 (1 - 8r^2 + 8r^6 - r^8 - 24r^4 \ln(r)), \quad r = \frac{M_N}{m_\mu}. \quad (8)$$

Here the integrated muon flux  $\Phi_{\mu^-}(E)$  is obtained by fitting the left-hand side of (5) with an assumption of power-low behavior of  $\Phi_{\mu^-}(E)$ . The same exercise is applied for  $\nu_e\text{-}\mu^+\text{-}N$  chain and then the flux for the Majorana  $N$  is obtained as the sum of these two contributions. Details for the energy distributions in muon decay are presented in Appendix A.1.

In the mass regime  $M_N < m_{\pi^\pm} - m_\mu$ , pions also contribute to the sterile neutrino flux. Roughly speaking,  $\pi^\pm$  contribution is the same as the muon contribution, so that the flux of the sterile neutrino in  $M_N < m_{\pi^\pm} - m_\mu$  regime is twice as large as the higher mass regime up to the threshold effect. The  $\pi^\pm$  contribution is estimated in the same way as the muon. For the  $\pi^\pm$  case, however, we need  $\nu_\mu, \bar{\nu}_\mu$  fluxes of  $\pi^\pm$  origin to reconstruct the integrated  $\pi^\pm$  fluxes from the muon neutrino input. We assess the  $\nu_\mu, \bar{\nu}_\mu$  of  $\pi^\pm$  origin by subtracting the  $\nu_\mu, \bar{\nu}_\mu$  of  $\mu^\pm$  origin from the full  $\nu_\mu, \bar{\nu}_\mu$  data in Ref. [20], where  $\nu_\mu, \bar{\nu}_\mu$  of  $\mu^\pm$  origin is calculated from the integrated muon fluxes  $\Phi_{\mu^\pm}(E)$  reconstructed via Eq. (5). Finally, the sterile neutrino flux of  $\pi^\pm$  origin is calculated by

$$\phi_N(E_N, t_f) = \frac{\Gamma'_\pi}{\Gamma_\pi} \int_{E_N}^{\infty} dE \Phi_{\pi^\pm}(E) \frac{1}{\Gamma'_\pi} \frac{d\Gamma'_\pi}{dE_N}(E, E_N), \quad (9)$$

where  $\Gamma_\pi$  and  $\Gamma'_\pi$  are the decay width for  $\pi^\pm \rightarrow \mu^\pm \nu_\mu(\bar{\nu}_\mu)$  and  $\pi^\pm \rightarrow \mu^\pm N$ , respectively. Here the branching ratio is given by

$$\frac{\Gamma'_\pi}{\Gamma_\pi} = |\Theta_\mu|^2 \sqrt{1 - 2(r_N^2 + r_\mu^2) + (r_N^2 - r_\mu^2)^2} \frac{r_N^2 + r_\mu^2 - (r_N^2 - r_\mu^2)^2}{r_\mu^2(1 - r_\mu^2)^2},$$

$$r_N = \frac{M_N}{m_{\pi^\pm}}, \quad r_\mu = \frac{m_\mu}{m_{\pi^\pm}}. \quad (10)$$

Fig. 1 shows the sterile neutrino fluxes for several examples of  $M_N$ . The six types of the lines are for  $M_N = 3, 10, 30, 40, 60, 80$  MeV, respectively (from the left). It is seen that a naive estimation  $\phi_N = |\Theta_\mu|^2 \phi_{\nu_\mu + \bar{\nu}_\mu}$  made in Ref. [17] is good for the energies above the mass threshold with  $M_N < 30$  MeV, but it breaks down significantly for  $M_N \gtrsim 30$  MeV in such a way that the calculated fluxes are suppressed as  $M_N$  increases. This rapid fall off with respect to  $M_N$  is due to the phase space suppression of the muon decay (See Eq. (8)). On the other hand, the phase space suppression of  $\pi^\pm$  decay is significant only at the vicinity of the threshold  $m_{\pi^\pm} - m_\mu$ . As  $M_N$  increases, the flux thus suddenly drops by factor of two at the threshold  $\approx 35$  MeV above which the  $\pi^\pm$  contribution vanishes. The sterile neutrino fluxes presented here are averaged over the zenith angle and given at the middle level of solar activity following the input neutrino fluxes in Ref. [20].

The uncertainty of the reconstructed parent fluxes  $\Phi_{\mu^\pm}$  and  $\Phi_{\pi^\pm}$  is small for high-energy regime, but it becomes larger as the energy is lowered so that the resultant sterile

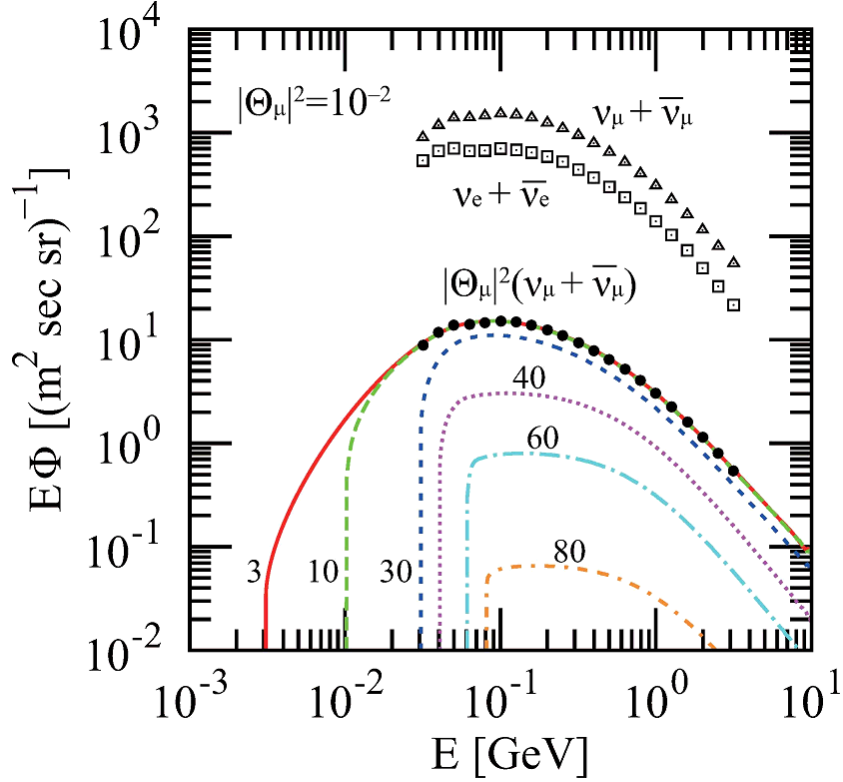


Figure 1: Fluxes of the sterile neutrinos. The six curves are for  $M_N = 3, 10, 30, 40, 60, 80$  MeV with the mixing  $|\Theta_\mu|^2 = 10^{-2}$ . The triangles and squares show the active neutrino fluxes from Ref. [20]. The black circles show  $|\Theta_\mu|^2\phi_{\nu_\mu+\bar{\nu}_\mu}$ .

neutrino fluxes carry certain ambiguity around  $E_N \simeq M_N$ . This is because high-energy part of the active neutrino flux is well fitted by a single-power law, while low-energy part are complex and many choices are available as fitting function. In this analysis, we have used the fitting function  $\Phi_H\Phi_L/(\Phi_H + \Phi_L)$ , where  $\Phi_H$  and  $\Phi_L$  are the high and low-energy part of the fitting function. For  $\Phi_H$ , we have taken  $\Phi_H = a_H\gamma^{b_H}$  with some constants  $a_H, b_H$  and the gamma factor  $\gamma$  of the parent particle of interest. For  $\Phi_L$ , we have examined two options  $\Phi_L = a_L\beta^{b_L}$  or  $\Phi_L = a_L\gamma^{b_L}$ , where  $\beta$  is the beta factor of the parent particle. While with the former  $\Phi_L$  the flux rises from the mass threshold and continuously shifts to constant behavior and is finally reduced to  $\Phi_H$ , the latter  $\Phi_L$  has discontinuity at the mass threshold and the peak is slightly shifted to lower energies compared with the former one. It turns out that two different fitting bring at most 10% difference in the total number of events. We would like to emphasize that the salient feature of the phase space suppression (8) is however independent from the fitting scheme and the conclusions derived from this effect are valid in what follows. The fluxes shown

in Fig. 1 are calculated with the option  $\Phi_L = a_L \beta^{b_L}$  and these fluxes are used in the following analyses.

### 3 Decay of the sterile neutrinos and the event rates

The sterile neutrinos  $N$  are produced in the atmosphere and reach the SK site to leave  $2e$ -like events via  $N \rightarrow e^- e^+ \nu$  and  $N \rightarrow e^+ e^- \bar{\nu}$ . Suppose that the fiducial volume of SK is represented by a sphere of radius  $r$ . The event rate is then given by

$$\text{Rate} = \int_{M_N}^{\infty} dE_N \int r^2 d\Omega \phi_N \int_l^{l+2r} dl' \frac{1}{\lambda_d} e^{-\frac{l'}{\lambda_d}} \int dX \frac{1}{\Gamma_N} \frac{d\Gamma_N}{dX}(E_N, X), \quad (11)$$

where  $\Gamma_N$  and  $\lambda_d$  are the decay width and length for the signal decay of  $N$ ,  $X$  is an observable of interest, *e.g.*, the invariant mass of the momentums of  $e^-$  and  $e^+$ , and  $l$  is the flight distance of the sterile neutrinos. The total decay length  $\Lambda_d$  is given by  $\Lambda_d = \lambda_d \lambda'_d / (\lambda_d + \lambda'_d)$  where  $\lambda'_d$  is the decay length for  $N \rightarrow 3\nu$ . Since  $r$  is much smaller than the earth radius  $R_{\oplus}$ , the flight distance  $l$  is well approximated by

$$l = \begin{cases} 0 & \text{for } 0 \leq \theta \leq \frac{\pi}{2}, \\ -2R_{\oplus} \cos \theta & \text{for } \frac{\pi}{2} < \theta \leq \pi, \end{cases} \quad (12)$$

in terms of the zenith angle  $\theta$ . The total events are given by the integration over the solid angle  $\int d\Omega = \int_{-1}^1 d\cos \theta \int_0^{2\pi} d\phi$ . By integrating over all possible final states of  $e^- e^+ \nu$  and taking  $\Lambda_d \gg 2r$ , Eq. (11) becomes

$$\text{Rate} = 3V_{\text{fid}} \int_{M_N}^{\infty} dE_N \frac{1}{\lambda_d} \phi_N \left[ \frac{\Lambda_d}{2R_{\oplus}} \left( 1 - e^{-\frac{2R_{\oplus}}{\Lambda_d}} \right) + 1 \right], \quad (13)$$

where  $V_{\text{fid}}$  is the fiducial volume of the SK tank 22.5kton which corresponds to  $2.25 \times 10^4 \text{ m}^3$ . Here the first (second) term in the square brackets is the contribution from the up (down)-going events. For  $\Lambda_d \gg 2R_{\oplus}$ , one finds

$$\text{Rate} = 6V_{\text{fid}} \int_{M_N}^{\infty} dE_N \frac{1}{\lambda_d} \phi_N, \quad (14)$$

which is independent from the total decay width and depends only on the partial decay width  $\Gamma_N$  responsible for the detection channel. The events take place isotropically due to the condition  $\Lambda_d \gg 2R_{\oplus}$  with which the flight distance  $l$  becomes irrelevant to the event number. While if  $\Lambda_d < 2R_{\oplus}$  so that the sterile neutrinos partially vanish on the way to the detector, downward-going events dominate over upward-going event. The measurements



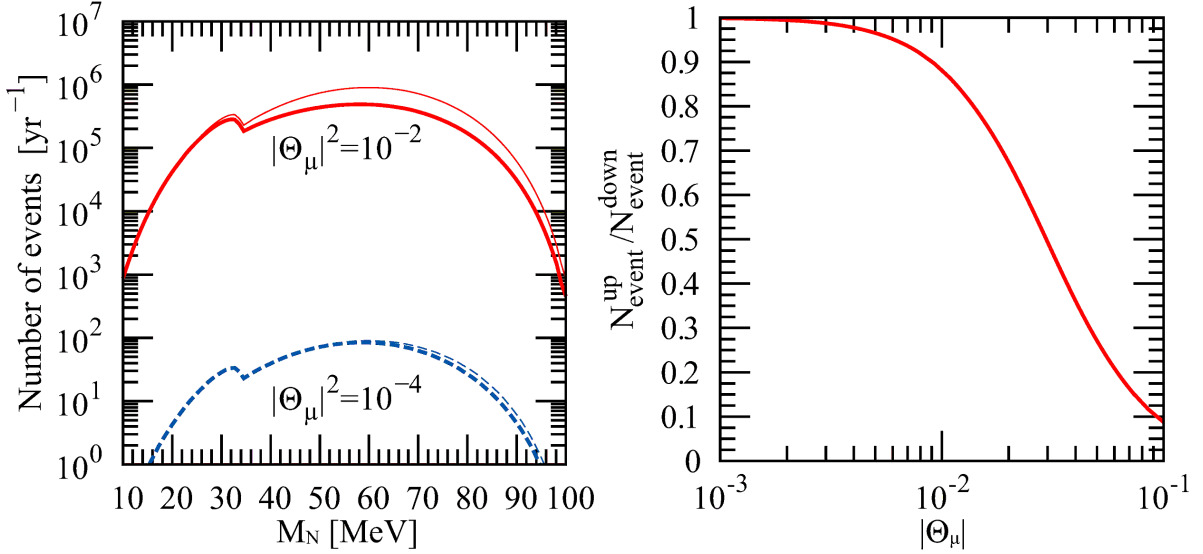


Figure 2: Left panel: Number of events ( $N \rightarrow e^-e^+\nu$ ) at SK per year. The red solid (blue dotted) lines shows the case when  $|\Theta_\mu|^2 = 10^{-2}(10^{-4})$ . The thick and thin lines are with and without the effect of  $N$  decay from atmosphere to detector. Right panel: Up-down asymmetry in number of events. Here we take  $M_N = 60$  MeV.

of the direction of the total momentum of  $e^-$  and  $e^+$  may thus clarify the indication of  $N \rightarrow 3\nu$  decay taking place on the way to the detector.

The left panel of Fig. 2 shows the total number of events per year as a function of the sterile neutrino mass  $M_N$ . The red solid (blue dotted) lines shows the case when  $|\Theta_\mu|^2 = 10^{-2}(10^{-4})$ . It is seen that the event number is proportional to  $|\Theta_\mu|^4$ . The thick and thin lines are with and without the effect of  $N$  decay from atmosphere to the detector. The thick lines are suppressed compared to the thin lines by the amount that the up-going events are reduced by the decay effect. The decay effect is negligible for  $|\Theta_\mu|^2 = 10^{-4}$  while it makes certain difference for  $|\Theta_\mu|^2 = 10^{-2}$ . The right panel shows the ratio of the up-going events to the down-going events. As we will see later, the asymmetry is unlikely to be observed for  $|\Theta_\mu|^2 \lesssim 3 \times 10^{-5}$  and  $M_N = 60$  MeV where the number of events does not exceed the  $2e$ -like ring data of SK.

If  $\Theta_\tau$  is switched on, however, it hastens both decay  $N \rightarrow 3\nu$  and  $N \rightarrow e^-e^+\nu$  while the production processes are kept unchanged. With  $\Theta_\tau$  being finite, the decay width of each mode is obtained by replacing  $|\Theta_\mu|^2$  with  $|\Theta_\mu|^2 + |\Theta_\tau|^2$  in (2) and (3). By virtue of  $\Theta_e = 0$ , the above two decay modes are induced only by the neutral current so that the effect of  $\Theta_\tau \neq 0$  simply appears as such a simple replacement. On the other hand, the production processes of  $N$  are not affected by  $\Theta_\tau$  since the decays of  $\pi^\pm$  and  $\mu^\pm$  are

induced by the charged current and cannot involve a tauon. Under the assumption that  $\Theta_e = 0$ , the production processes thus involve only  $\Theta_\mu$ . In the flux equation (6), the decay term of  $N$  would not be negligible if  $|\Theta_\tau|$  is large. This effect however gives negligible contribution to the ratio of upward to downward-going events since the thickness of the atmosphere is small compared to the earth's diameter.

An interesting possibility in view of the up-down asymmetry is therefore  $|\Theta_\tau| \gg |\Theta_\mu|$  with which the flux is feeble while the decay probability is high. In such case the event rate is proportional to  $|\Theta_\mu|^2 |\Theta_\tau|^2$  instead of  $|\Theta_\mu|^4$ , where  $|\Theta_\mu|^2$  comes from the production and  $|\Theta_\tau|^2$  is from the detection. Let us set  $|\Theta_\mu|^2 |\Theta_\tau|^2 \sim 10^{-9}$  to obtain  $\mathcal{O}(10)$  events per year. Then, for instance,  $|\Theta_\tau|^2 \sim 10^{-2}$  and  $|\Theta_\mu|^2 \sim 10^{-7}$  lead to a clear asymmetry  $N^{\text{up}}/N^{\text{down}} \sim 0.1$ . (Notice that the right panel of Fig. 2 can be read as a plot for  $|\Theta_\tau|$  in the case where  $|\Theta_\tau| \gg |\Theta_\mu|$ .) If the asymmetry is observed, it may indicate a hierarchical structure of  $|\Theta_\tau| \gg |\Theta_\mu|$ .

The master formula for the event rate (11) involves the product of the production and the detection probabilities. That is, the product of the squared modulus of the production and the detection amplitudes. This means that (11) is valid in the case where the coherence between the propagating neutrino states is lost. Since we have the sterile neutrino and the active neutrinos in the theory, one may wonder if the oscillation between the active and sterile states occurs. However, the coherence between the active and sterile states is explicitly violated at the detection point; the sterile neutrino decays while the active neutrinos do not. Furthermore, even if the coherence were not violated by the detection, such an oscillation would be so rapid that the effect is averaged out, which also insures the validity of using (11). In fact, with  $M_N = 10$  MeV and a typical energy of 100 MeV for example, the oscillation length  $L^{\text{ocs}}$  would be  $L^{\text{ocs}} \simeq \left(\frac{E}{100 \text{ MeV}}\right) \left(\frac{100 \text{ MeV}^2}{\Delta m^2}\right) 10^{-12}$  m. In the present setup, it is quite difficult to observe oscillatory behavior between the active and the sterile neutrinos.

### 3.1 Invariant mass and bounds for the mixing

The sterile neutrino decay  $N \rightarrow e^- e^+ \nu$  in the SK detector produces two fuzzy Cherenkov rings. A possible background for this signal is  $\pi^0 \rightarrow 2\gamma$ , where  $\pi^0$  are mainly created via the neutral current interactions of the atmospheric active neutrinos. The gamma rays in the final state develop into electromagnetic showers and create two fuzzy rings which cannot be distinguished from the  $e^\pm$  signals.

The above two process, however, leave different signatures in the Lorentz invariant

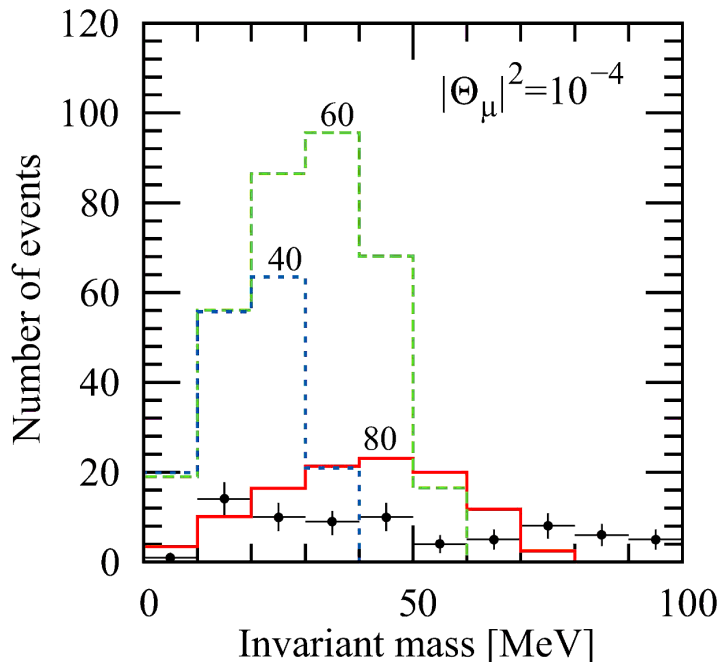


Figure 3: Invariant mass distribution of the electron pairs from the sterile neutrino decay  $N \rightarrow e^-e^+\nu$ . The solid (red), dashed (green), and short-dashed (blue) lines are for  $M_N = 80, 60, 40$  MeV with the mixing  $|\Theta_\mu|^2 = 10^{-4}$ . The points with error bars are the data of fully-contained  $2e$ -like rings from Ref. [18].

mass (squared) of the  $2e$ -like rings. For the sterile neutrino event  $N \rightarrow e^-e^+\nu$ , it is given by  $M_{ee}^2 = (p_1 + p_2)^2$ , where  $p_1(p_2)$  are the four-momenta of  $e^-(e^+)$ . In the rest frame of the sterile neutrino, it reads

$$M_{ee}^2 \simeq M_N^2 - 2M_N E_\nu, \quad (15)$$

where  $E_\nu$  is the invisible energy carried away by the active neutrino. Since the neutrino carries about 1/3 of the parent energy on average,  $M_{ee}^2$  from the sterile neutrino events follows  $\langle M_{ee}^2 \rangle \simeq M_N^2/3$ , while the invariant mass squared of the two photons by  $\pi^0$  decay sharply peaks at  $m_{\pi^0}^2$ . By measuring the invariant mass distribution, we may obtain information on the sterile neutrino mass.

It is more practical to work with  $M_{ee}$  than  $M_{ee}^2$ . The  $M_{ee}$  distribution is given by (See Appendix A.3 for details)

$$\frac{1}{\Gamma_N} \frac{d\Gamma_N}{dM_{ee}} = \frac{4}{M_N} y_{ee} (1 - y_{ee}^2)^2 (1 + 2y_{ee}^2), \quad (16)$$

where  $y_{ee} = M_{ee}/M_N$ . The distribution (16) has the maximum at  $y_{ee} \sim 0.5$ , and the averaged invariant mass is given by  $\langle M_{ee} \rangle = \int_0^{M_N} dM_{ee} \frac{M_{ee}}{\Gamma_N} \frac{d\Gamma_N}{dM_{ee}} = 0.508 M_N$ . Note that the

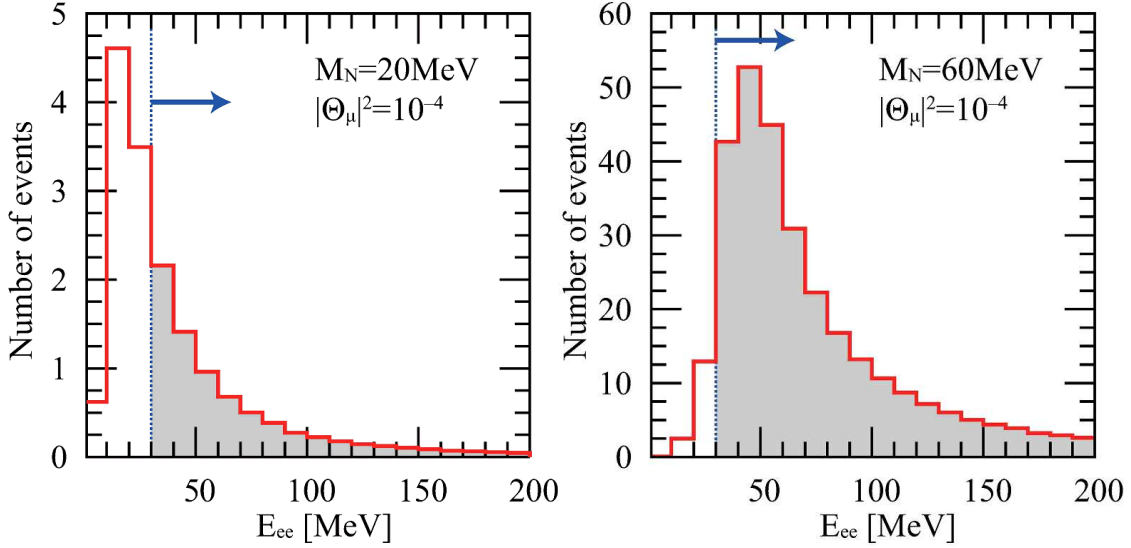


Figure 4: Visible energy distributions for  $M_N = 20$  MeV (left) and  $M_N = 60$  MeV (right). Here we take  $|\Theta_\mu|^2 = 10^{-4}$ .

distribution function (16) also holds in the laboratory frame due to the Lorentz invariance of  $M_{ee}^2$ . We calculate the event rate for each invariant mass by using (16) in (11).

Fig. 3 shows the number of events in each invariant mass bin. The solid (red), dashed (green), and short-dashed (blue) lines are for  $M_N = 80, 60, 40$  MeV with the mixing  $|\Theta_\mu|^2 = 10^{-4}$ . The points with error bars are the 1489 days data of fully-contained  $2e$ -like rings from Ref. [18]. Following (16), the events are distributed to the range  $0 < M_{ee} < M_N$  and frequently seen at  $\simeq 0.5M_N$ . From  $M_N = 40$  MeV to  $M_N = 60$  MeV, the height of the peak grows although the possible range of  $M_{ee}$ , to which the events are distributed, is broadened. This is because the total number of event increases from  $M_N = 40$  MeV to  $M_N = 60$  MeV (see Fig. 2). On the other hand, the height of the peak rapidly falls off from  $M_N = 60$  MeV to  $M_N = 80$  MeV since not only the range of  $M_{ee}$  is broadened but also the total number of event decreases.

A naive upper bound for  $\Theta_\mu$  would be determined by comparing the height of each bin with the corresponding background for fixed values of  $M_N$ . However, it should be noticed that the SK data shown in Fig. 3 is for visible energy greater than 30 MeV, where the visible energy means the total energy of the two rings (hereafter we denote it by  $E_{ee}$ ). Hence we must cut the events whose  $E_{ee}$  is less than 30 MeV to make such a comparison. In addition, In addition, the opening angle between two momenta of  $e^-$  and  $e^+$  must be sufficiently large in order for the event to be identified as multi-ring events. Thus one must

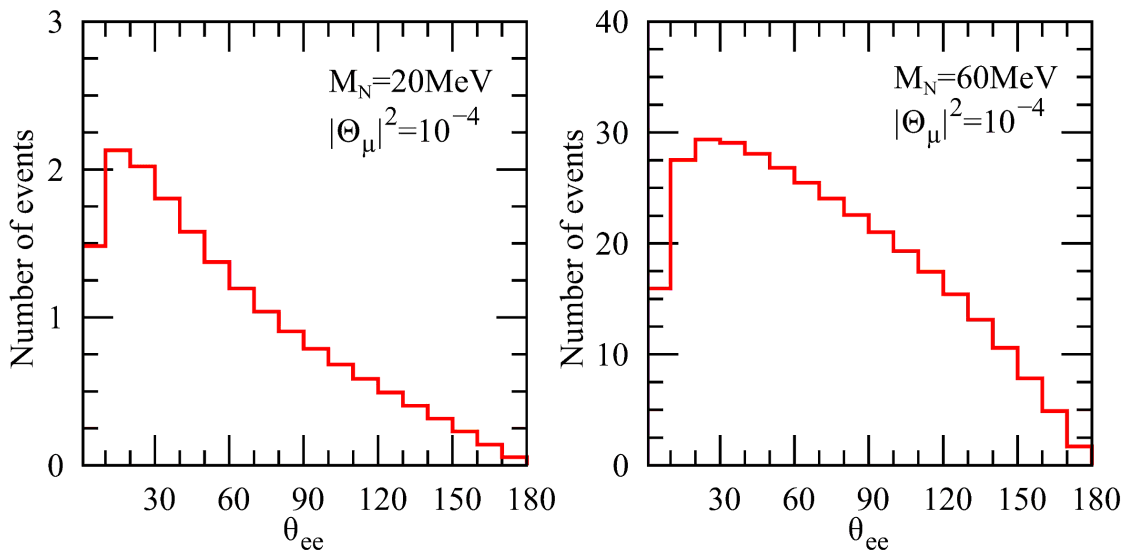


Figure 5: Opening angle  $\theta_{ee}$  distributions for  $M_N = 20$  MeV (left) and  $M_N = 60$  MeV (right). Here we take  $|\Theta_\mu|^2 = 10^{-4}$ .

study how  $E_{ee}$  and the angle cut reduce the number of events for a reasonable estimation of the allowed parameter range.

Roughly speaking, the two cut define an effective range of the sterile neutrino energy  $E_N$  for a given value of  $M_N$ . In particular, the visible-energy cut defines a lower limits of  $E_N$ . In the three-body decay  $N \rightarrow e^-e^+\nu$ , the electron and positron carry on average about 1/3 of the parent energy each, so that the events with  $E_N \gtrsim 45$  MeV more or less pass the cut. Accordingly, the number of event receives significant reduction for  $M_N \lesssim 45$  MeV while it does not for  $M_N \gtrsim 45$  MeV. Fig. 4 shows two examples of  $E_{ee}$  distributions. It is seen that about 60% of the whole event is dropped for  $M_N = 20$  MeV but the cut is insignificant for  $M_N = 60$  MeV.

On the other hand, the angle cut does not dramatically change the number of events. In Fig. 5, we show the opening-angle distributions for  $M_N = 20$  MeV and  $M_N = 60$  MeV, assuming angle resolution of  $10^\circ$ . It is clear that the angle cut does not have as much impact as the visible energy cut for both cases if the two rings with  $\theta_{ee} \gtrsim 10^\circ$ , or more conservatively,  $\theta_{ee} \gtrsim 20^\circ$ , can be separately identified at SK. We found that efficiencies of the angle cut are 0.65 for  $M_N = 10$  MeV, 0.8 for  $M_N = 20$  MeV and 0.85 for  $M_N = 30 - 100$  MeV with  $\theta_{ee} > 20^\circ$ . The sterile neutrinos with smaller mass receives more reduction than larger mass since light sterile neutrinos are more energetic. It is seen in Fig. 1 that sterile neutrinos are mostly populated in  $\gamma \sim 4 - 5$  for  $M_N = 20$  MeV while  $\gamma \sim 1 - 2$  for  $M_N = 60$  MeV.

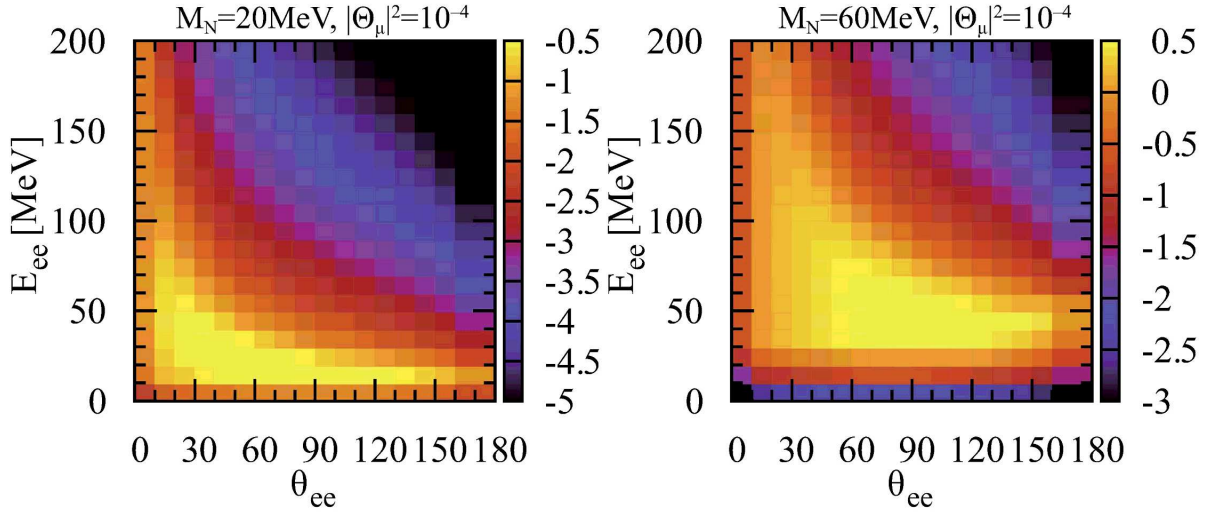


Figure 6: Correlation between  $E_{ee}$  and  $\theta_{ee}$  for  $M_N = 20$  MeV (left) and  $M_N = 60$  MeV (right). The colors in each bin shows  $\log_{10}(\text{number of events})$ .  $|\Theta_\mu|^2 = 10^{-4}$  is taken.

We present correlations between  $E_{ee}$  and  $\theta_{ee}$  in Fig. 6 for completeness. For a lighter mass  $M_N = 20$  MeV, most sterile neutrinos are energetic  $\gamma \sim 4 - 5$  and the events are concentrated on lower-left region. For the heavier mass  $M_N = 60$  MeV, the peak is shifted toward larger  $\theta_{ee}$  region since there are many sterile neutrinos with  $\gamma \sim 1$ , and  $\theta_{ee}$  tends to be close to  $\sim 120^\circ$  expected from the decay at rest. We would like to emphasize that these plots may be useful to separate the signal from the background if the tendency of the background is different from the signal.

Having details for the visible energy and the opening angle distribution, let us come back to the invariant mass and estimate the upper bound of the mixing element  $\Theta_\mu$ . Fig. 7 shows the invariant mass distributions of events with a kinematical cut. As is already mentioned, lighter-mass case receives more significant reduction by the cuts. We would like to stress that, while the visible energy cut  $E_{ee} \geq 30$  MeV is indeed applied to the SK data, the angle cut is not the actual one which is applied to the data. In fact, the multi-ring identification process performed in the SK analysis [25] is much more complicated than the selection of opening angles and such a thorough analysis is beyond the scope of this paper. Since we do not know the minimal opening angle appropriate for the SK detector and could not find suitable references for this value, here and henceforth we assume it to be  $20^\circ$  just for example. We estimate the upper bound for  $\Theta_\mu$  by searching for the maximal value of  $\Theta_\mu$  with which none of the signal events of each bin exceeds the central value of the data [18] (shown by dots with error bars in the figures) for each fixed

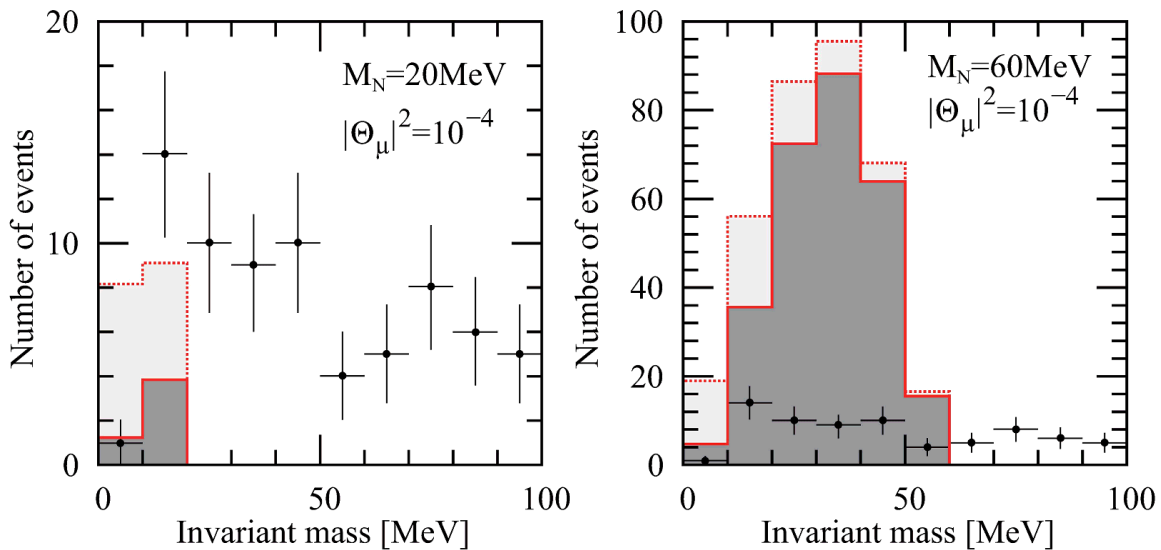


Figure 7: Invariant mass distributions of events at SK for  $M_N = 20$  MeV (left) and  $M_N = 60$  MeV (right). The light gray region with red dotted line is without cuts, while the dark gray region with red solid line is with  $\theta_{ee} \geq 20^\circ$  and  $E_{ee} \geq 30$  MeV.

value of  $M_N$ .

Fig. 8 shows the upper bound in comparison with the previous result in Ref. [17]. The bound is changed in three ways. First of all, in the large-mass region  $M_N \gtrsim 50$  MeV, the bound is significantly relaxed due to the phase space suppression of the muon decay which has not been taken into account in the previous analysis. Second, in the small-mass region  $M_N \lesssim 50$  MeV, the event cuts (mainly the visible energy cut  $E_{ee} > 30$  MeV) reduce the number of events so that the bound is pushed up from the curve without the cuts. Finally, careful handling of the  $\pi^\pm$  and  $\mu^\pm$  contributions for the sterile neutrino production makes a small dip at  $M_N = m_{\pi^\pm} - m_\mu$  since the number of events are reduced for  $M_N > m_{\pi^\pm} - m_\mu$  according to the absence of the  $\pi^\pm$  contributions.

The light-element abundances predicted by the Big Bang Nucleosynthesis (BBN) is kept unspoiled if the lifetime of  $N$  is short enough such that the sterile neutrinos are cleared away before the onset of the BBN. According to Ref. [22], the successful BBN requires

$$|\Theta_\alpha|^2 > 568.4 \left( \frac{M_N}{\text{MeV}} \right)^{-3.549} - 5.17 \times 10^{-6}, \quad (\alpha = \mu, \tau), \quad (17)$$

for  $10 \text{ MeV} < M_N < 140 \text{ MeV}$ . Here this limit is valid for the Dirac type sterile neutrino which mixes with only one active flavor. For the Majorana case, this limit becomes two times weaker since the total decay width of the Majorana particle involves an extra factor

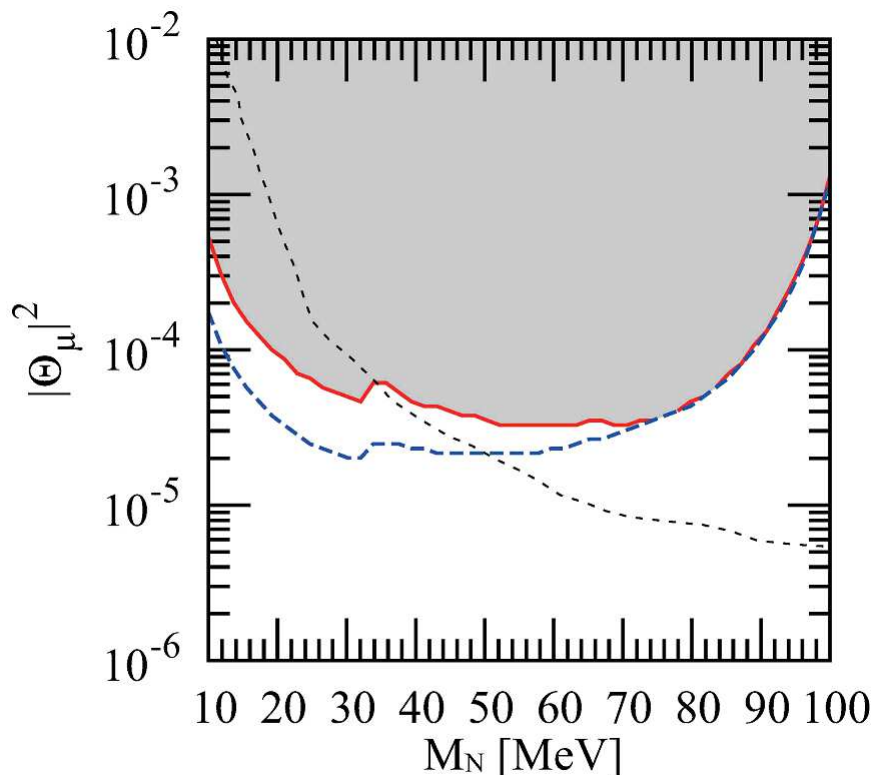


Figure 8: Upper bounds on the mixing element  $|\Theta_\mu|^2$ . The red solid and blue dashed lines are bounds with and without cuts  $\theta_{ee} \geq 20^\circ$  and  $E_{ee} \geq 30$  MeV, respectively. The black dotted line shows the bound in Ref. [17].

of two. Most of the allowed region in Fig. 8 is in fact under tension with the limit (17). However, this tension is relaxed if  $\Theta_\tau$  is turned on. Namely, the lifetime is shortened by increasing  $|\Theta_\tau|$ . The point is that the production of the sterile neutrino in the atmosphere is not affected by  $|\Theta_\tau|$ . Hence, by taking  $|\Theta_\tau| \gg |\Theta_\mu|$ , one can set a short lifetime enough to avoid the BBN limit while keeping the atmospheric sterile neutrinos consistent with the SK data. Notice that Fig. 8 can be read as a plot for  $|\Theta_\mu||\Theta_\tau|$  if  $|\Theta_\tau| \gg |\Theta_\mu|$ . Interestingly, the directional asymmetry (see Fig. 2 and related discussion) is likely to be observed in such a circumstance.

If the visible energy cut  $E_N > 30$  MeV is switched off, the sterile neutrino events in the first three bins increase as shown in Fig. 7, while the background and its Monte Carlo simulation might change differently depending on the source of the background. Such an analysis is important especially for light sterile neutrinos with  $M_N < 30$  MeV but beyond the scope of this paper.



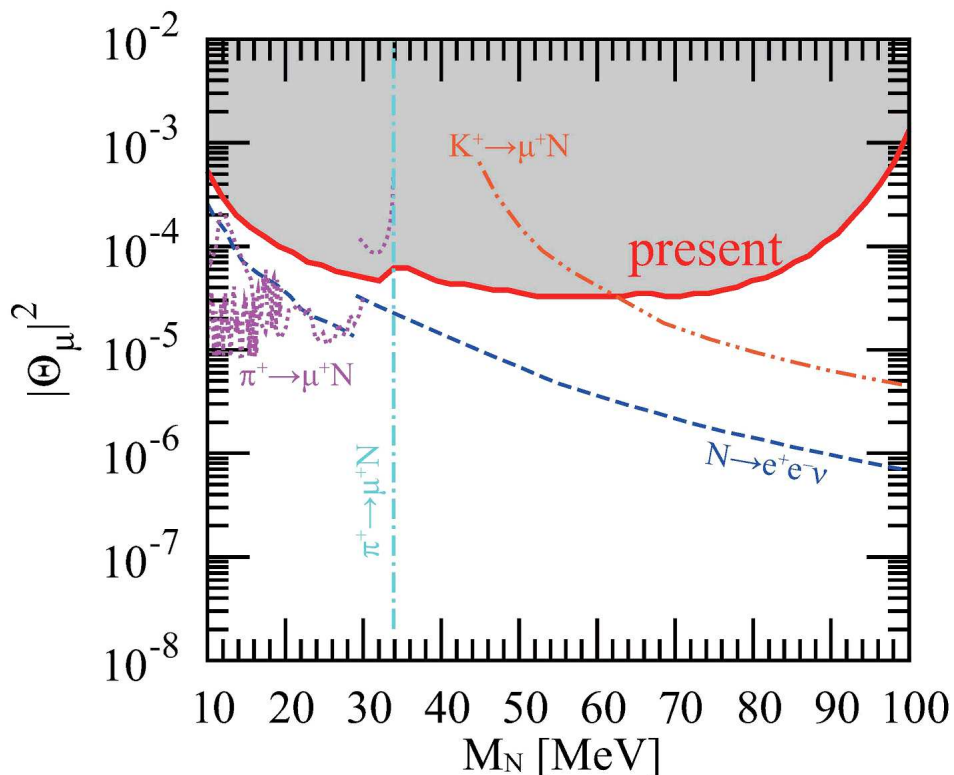


Figure 9: Upper bounds on the mixing element  $|\Theta_\mu|^2$  (the red solid curve) in comparison with various experiments. The dotted (purple) curve is from the peak search in pion decay [11] (labeled by  $\pi^+ \rightarrow \mu^+ N$ ), the dot-dashed (light-blue) line is from the peak search in pion decay [12], the dashed curve (blue) is from the accelerator decay search by PS191 [16] (labeled by  $N \rightarrow e^+ e^- \nu$ ), and the dot-dot-dashed (orange) curve is from the peak search in kaon decay [14] (labeled by  $K^+ \rightarrow \mu^+ N$ ).

## 4 Conclusions

We have studied the production and the detection of the atmospheric sterile neutrinos. With the mass range  $1 \text{ MeV} \lesssim M_N \lesssim 105 \text{ MeV}$ , the sterile neutrinos are produced by muon or pion decays. The main decay mode of the sterile neutrino  $N$  is  $N \rightarrow 3\nu$  (88%) and the subdominant mode is  $N \rightarrow e^- e^+ \nu$  (12%). Interestingly, the detection via the subdominant channel is feasible at Super-Kamiokande. To estimate the amount of the sterile neutrino flux  $\phi_N$ , we have reconstructed the parent muon and pion integrated fluxes from the well-established active neutrino fluxes  $\phi_\nu$  by making a power-law ansatz for the shape of the spectrum. We have calculated the sterile neutrino flux from the reconstructed parent fluxes and the energy distributions of each decay mode. The phase space suppression of the muon decay  $\mu^\pm \rightarrow e^\pm \nu_e(\bar{\nu}_e) N$  is so effective that the estimated

sterile neutrino flux is much less than the naive expectation of  $\phi_N = |\Theta_\mu|^2 \phi_{\nu+\bar{\nu}_\mu}$  for  $M_N \gtrsim 40$  MeV.

For the detection, we have calculated the number of the decay event  $N \rightarrow e^- e^+ \nu$  at SK. The upper bound for the muon-type mixing  $\Theta_\mu$  is estimated by comparing the invariant mass distribution of the  $e^\pm$  pair and the observational data of the  $2e$ -like rings. To estimate the bound, the visible energy cut  $E_N > 30$  MeV is taken into account in accordance with the SK data. Moreover, we have studied the opening angle of the  $e^\pm$  momenta and clarify the impact of the minimal opening angle under which the two fuzzy rings cannot be identified separately. The upper bound for higher mass regime  $M_N \gtrsim 50$  MeV is significantly relaxed compared to the previous estimation due to the phase space suppression of the muon decay. In addition, the inclusion of the kinematical cuts also relaxes the bound for lower mass regime and changes the shape of the bound entirely.

Fig. 9 shows the upper bound in comparison with the other experiments (see for example, Ref. [23, 24]). In the mass window of  $34 \text{ MeV} < M_N \lesssim 64 \text{ MeV}$ , the atmospheric bound is stronger than the peak search in the meson decays. However, the bound from the accelerator decay search<sup>†</sup> is stronger than the atmospheric bound by a factor of two at  $M_N = 34$  MeV and by a factor of 10 at  $M_N = 64$  MeV. We nevertheless believe that the search for the atmospheric sterile neutrino is an issue of great interest. One reason is that not a few progresses in particle physics have been made in cooperation between artificial and natural source experiments. Since PS191 is the sole experiment which set the bound stronger than the atmospheric one in the window  $34 \text{ MeV} < M_N \lesssim 64 \text{ MeV}$ , the atmospheric sterile neutrino can play a role of a unique follow-up experiment with a natural source.

Moreover, many points are to be ameliorated for better sensitivities of the atmospheric sterile neutrino. It is obvious that our naive scheme to estimate the upper bound does not reflect the accumulation of statistics and more advanced analysis should be performed for precise argument. The  $2e$ -like ring data for SKI, SKII and SKIII [25] can be combined to squeeze the room remained for the sterile neutrino. Furthermore, the analysis of the  $2e$ -like events can be customized aiming for the sterile neutrino detection. For instance, one can switch off the visible energy cut of 30 MeV and track the direction of the sum of the two ring's momenta, the opening angle between two rings and the visible energy. This may dramatically change the sensitivity if the background behaves differently from the

---

<sup>†</sup> We have included the neutral current contribution to  $N \rightarrow e^- e^+ \nu$  to apply the bound from Ref. [16]. See Ref. [17, 24].

signal in the up/down-going ratio, opening angle distribution, visible energy distribution and so on. As for the detection facility, Hyper-Kamiokande has been proposed with the fiducial volume 25 time larger than SK [26], and hence the number of events increases by the same amount, which improve the bound, roughly speaking, by a factor of five. If the new customized analysis upgrades the sensitivity for  $|\Theta_\mu|^2$  by a factor of two for instance, Hyper-Kamiokande will improve the bound by one order of magnitude and will reach the present accelerator bound. With the refinement of the analysis and the upgrade of the facility, there will be a good chance to discover the atmospheric sterile neutrino.

## Acknowledgments

We would like to thank Particle and Astroparticle Division of Max-Planck-Institut für Kernphysik at Heidelberg for hospitality. The works of T.A. and A.W. are supported by the Young Researcher Overseas Visits Program for Vitalizing Brain Circulation Japanese in JSPS (No. R2209). T.A. is also supported by KAKENHI (No. 21540260) in JSPS.

## A Details for the decay processes

For the sake of completeness, we present here necessary formulas for the decay processes to produce the results in Section 2 and 3. In this Appendix, we flexibly use the symbol  $\gamma$  and  $x$  to denote the gamma factor of the parent particles and (twice of) the daughter energy in unit of the parent mass. The electron mass is neglected in the following formulas.

### A.1 $\mu^- \rightarrow e^- \bar{\nu}_e N$

This decay process is conducted by the charged-current. In the laboratory frame, the decay width  $\Gamma'$  is

$$\Gamma' = \frac{G_F^2 m_\mu^5 |\Theta_\mu|^2}{192\pi^3} I_0 \left( \frac{1}{\gamma} \right), \quad (18)$$

where

$$I_0 = \left[ 1 - 8r^2 + 8r^6 - r^8 - 24r^4 \ln(r) \right], \quad r = \frac{M_N}{m_\mu}, \quad \gamma = \frac{E_\mu}{m_\mu}. \quad (19)$$

Here  $E_\mu$  is the muon energy in the laboratory frame. The energy distribution of the sterile neutrino  $N$  is given by (with  $x = 2E_N/m_\mu$ )

$$\frac{1}{\Gamma'} \frac{d\Gamma'}{dx} = g(\gamma, x) = \begin{cases} g_{\text{low}}(\gamma, x) & (1 < \gamma < \gamma_{\text{cr}}, x^- < x < x^c) \\ g_{\text{high}}(\gamma, x) & (1 < \gamma < \gamma_{\text{cr}}, x^c < x < x^+) \\ g_{\text{high}}(\gamma, x) & (\gamma_{\text{cr}} < \gamma, x^- < x < x^+) \\ 0 & (\text{all others}) \end{cases}, \quad (20)$$

where

$$\begin{aligned} x^- &= 2r, & x^c &= \gamma(1+r^2) - \gamma\beta(1-r^2), & x^+ &= \gamma(1+r^2) + \gamma\beta(1-r^2), \\ \gamma_{\text{cr}} &= \frac{1+r^2}{2r}. \end{aligned} \quad (21)$$

The functions  $g_{\text{low}}$  and  $g_{\text{high}}$  are given by

$$\begin{aligned} g_{\text{low}}(\gamma, x) &= \frac{2\sqrt{x^2 - 4r^2}}{3I_0} \left[ (2 - 8\gamma^2)x^2 + 9(1+r^2)\gamma x + 4r^2(2\gamma^2 - 5) \right], \\ g_{\text{high}}(\gamma, x) &= \frac{1}{6I_0\sqrt{\gamma^2 - 1}} \left[ (1+r^2)(5 + (36\gamma^2 - 50)r^2 + 5r^4) + 24r^2\gamma(3 - 2\gamma^2)x \right. \\ &\quad \left. - 9(2\gamma^2 - 1)(1+r^2)x^2 + 4\gamma(4\gamma^2 - 3)x^3 \right] + \frac{1}{2}g_{\text{low}}(\gamma, x). \end{aligned} \quad (22)$$

## A.2 $\pi^+ \rightarrow \mu^+ N$

The decay width in the laboratory frame is

$$\Gamma'_\pi = \frac{G_F^2 f_\pi^2 m_{\pi^\pm}^3 |V_{ud}|^2 |\Theta_\mu|^2}{8\pi} \beta_f \left[ r_N^2 + r_\mu^2 - (r_N^2 - r_\mu^2)^2 \right] \left( \frac{1}{\gamma} \right), \quad (23)$$

where

$$\beta_f = \sqrt{1 - 2(r_N^2 + r_\mu^2) + (r_N^2 - r_\mu^2)^2}, \quad r_N = \frac{M_N}{m_{\pi^\pm}}, \quad r_\mu = \frac{m_\mu}{m_{\pi^\pm}}, \quad \gamma = \frac{E_\pi}{m_{\pi^\pm}}. \quad (24)$$

The energy distribution of the sterile neutrino is given by (with  $x = 2E_N/m_{\pi^\pm}$ )

$$\frac{1}{\Gamma'_\pi} \frac{d\Gamma'_\pi}{dx} = \begin{cases} \frac{1}{2\beta_f} \frac{1}{\sqrt{\gamma^2 - 1}} & (1 < \gamma, x^- < x < x^+) \\ 0 & (\text{all others}) \end{cases}, \quad (25)$$

where

$$x^\pm = (1 + r_N^2 - r_\mu^2)\gamma \pm \beta_f \sqrt{\gamma^2 - 1}. \quad (26)$$

### A.3 $N \rightarrow e^- e^+ \nu_\alpha$ ( $\alpha = \mu, \tau$ )

This process is conducted by the neutral current if  $\Theta_e$  contribution is negligible. In this case, the decay width in the laboratory frame is given by

$$\Gamma_N = \frac{G_F^2 |\Theta_\alpha|^2 M_N^5}{192\pi^3} \left( \frac{1}{4} - \sin^2 \theta_W + 2 \sin^4 \theta_W \right) \left( \frac{1}{\gamma} \right). \quad (27)$$

In terms of the invariant mass  $M_{ee}^2$ , the visible energy  $E_{ee}$  and the opening angle of  $e^\pm$  momenta  $\theta_{ee}$ , the differential decay width is written as

$$\frac{1}{\Gamma_N} \int d\Gamma_N = \int_0^1 dz_{ee} \int_{x_v^-}^{x_v^+} dx_v \int_{-1}^{1 - \frac{8z_{ee}}{x_v^2}} d\cos \theta_{ee} J(z_{ee}, x_v, \cos \theta_{ee}) K(\gamma, z_{ee}, x_v, \cos \theta_{ee}), \quad (28)$$

where

$$z_{ee} = \frac{M_{ee}^2}{M_N^2}, \quad x_v = \frac{2E_{ee}}{M_N}, \quad \gamma = \frac{E_N}{M_N}, \quad x_v^\pm = \gamma(1 + z_{ee}) \pm \sqrt{\gamma^2 - 1}(1 - z_{ee}), \quad (29)$$

and

$$J(z_{ee}, x_v, \cos \theta_{ee}) = \frac{4z_{ee}}{\sqrt{x_v^2 - 4z_{ee}} \sqrt{x_v^2(1 - \cos \theta_{ee})^4 - 8z_{ee}(1 - \cos \theta_{ee})^3}}, \quad (30)$$

$$K(\gamma, z_{ee}, x_v, \cos \theta_{ee}) = \frac{3z_{ee}}{\sqrt{\gamma^2 - 1}(1 - \cos \theta_{ee})(x_v^2 - 4z_{ee})^2} \left[ f_0 + f_1 \cos \theta_{ee} \right]. \quad (31)$$

Here  $f_0$  and  $f_1$  are

$$\begin{aligned} f_0 &= 4z_{ee} (3 + 2(10\gamma^2 - 1)z_{ee} - z_{ee}^2) - 40\gamma z_{ee}(1 + z_{ee})x_v \\ &\quad + 4z_{ee} ((3 - 2\gamma^2) + 2z_{ee}) x_v^2 + 4\gamma(1 + z_{ee})x_v^3 - (1 + z_{ee})x_v^4, \end{aligned} \quad (32)$$

$$\begin{aligned} f_1 &= 4z_{ee} (-1 + 2(2\gamma^2 - 1)z_{ee} + 3z_{ee}^2) - 8\gamma z_{ee}(1 + z_{ee})x_v \\ &\quad + 4(1 + (2\gamma^2 + 1)z_{ee} - z_{ee}^2) x_v^2 - 4\gamma(1 + z_{ee})x_v^3 + (1 + z_{ee})x_v^4. \end{aligned} \quad (33)$$

By integrating over  $\cos \theta_{ee}$ , one finds for instance

$$\begin{aligned} \frac{1}{\Gamma_N} \frac{d\Gamma_N}{dz_{ee} dx_v} &= \frac{1}{\sqrt{\gamma^2 - 1}} (1 - z_{ee})(1 + 2z_{ee}) \quad (1 < \gamma, 0 < z_{ee} < 1, x_v^- < x_v < x_v^+), \\ \frac{1}{\Gamma_N} \frac{d\Gamma}{dz_{ee}} &= 2(1 - z_{ee})^2(1 + 2z_{ee}) \quad (0 < z_{ee} < 1). \end{aligned} \quad (34)$$

It is now straightforward to obtain (16) from (34). The analytical expressions for  $\theta_{ee}$  distribution are rather lengthy and we do not present them here.

## References

- [1] P. Minkowski, Phys. Lett. B **67** (1977) 421; T. Yanagida, in *Proc. of the Workshop on the Unified Theory and the Baryon Number in the Universe*, Tsukuba, Japan, Feb. 13-14, 1979, p. 95, eds. O. Sawada and S. Sugamoto, (KEK Report KEK-79-18, 1979, Tsukuba); Progr. Theor. Phys. **64** (1980) 1103 ; M. Gell-Mann, P. Ramond and R. Slansky, in *Supergravity*, eds. P. van Nieuwenhuizen and D. Z. Freedman (North Holland, Amsterdam 1980); P. Ramond, in *Talk given at the Sanibel Symposium*, Palm Coast, Fla., Feb. 25-Mar. 2, 1979, preprint CALT-68-709 (retroprinted as hep-ph/9809459); S. L. Glashow, in *Proc. of the Cargèse Summer Institute on Quarks and Leptons*, Cargèse, July 9-29, 1979, eds. M. Lévy et. al. , (Plenum, 1980, New York), p707; R. N. Mohapatra and G. Senjanovic, Phys. Rev. Lett. **44** (1980) 912.
- [2] M. Fukugita and T. Yanagida, Phys. Lett. B **174** (1986) 45.
- [3] S. Dodelson, L. M. Widrow, Phys. Rev. Lett. **72** (1994) 17-20; X. -D. Shi, G. M. Fuller, Phys. Rev. Lett. **82** (1999) 2832-2835; A. D. Dolgov, S. H. Hansen, Astropart. Phys. **16** (2002) 339-344; K. Abazajian, G. M. Fuller, M. Patel, Phys. Rev. **D64** (2001) 023501; K. Abazajian, G. M. Fuller, W. H. Tucker, Astrophys. J. **562** (2001) 593-604; T. Asaka, M. Laine and M. Shaposhnikov, JHEP **0606** (2006) 053; JHEP **0701** (2007) 091; M. Laine, M. Shaposhnikov, JCAP **0806** (2008) 031.
- [4] T. Asaka, S. Blanchet, M. Shaposhnikov, Phys. Lett. **B631** (2005) 151-156.
- [5] A. Kusenko, G. Segre, Phys. Lett. **B396** (1997) 197-200; Phys. Rev. **D59** (1999) 061302; G. M. Fuller, A. Kusenko, I. Mocioiu, S. Pascoli, Phys. Rev. **D68** (2003) 103002; M. Barkovich, J. C. D'Olivo, R. Montemayor, Phys. Rev. **D70** (2004) 043005; A. Kusenko, Int. J. Mod. Phys. **D13** (2004) 2065-2084; A. Kusenko, B. P. Mandal, A. Mukherjee, Phys. Rev. **D77** (2008) 123009.
- [6] E. K. Akhmedov, V. A. Rubakov, A. Y. Smirnov, Phys. Rev. Lett. **81** (1998) 1359-1362.
- [7] T. Asaka, M. Shaposhnikov, Phys. Lett. **B620** (2005) 17-26.

- [8] M. Shaposhnikov, JHEP **0808** (2008) 008; T. Asaka, H. Ishida, Phys. Lett. **B692** (2010) 105-113; L. Canetti and M. Shaposhnikov, JCAP **1009**, 001 (2010); T. Asaka, S. Eijima and H. Ishida, arXiv:1112.5565 [hep-ph].
- [9] D. Gorbunov and M. Shaposhnikov, JHEP **0710** (2007) 015.
- [10] R. E. Shrock, Phys. Rev. **D24** (1981) 1232; F. P. Calaprice, D. F. Schreiber, M. B. Schneider, M. Green, R. E. Pollock, Phys. Lett. **B106** (1981) 175-178; R. C. Minehart, K. O. H. Ziock, R. Marshall, W. A. Stephens, M. Daum, B. Jost, P. R. Kettle, Phys. Rev. Lett. **52** (1984) 804-807; M. Daum, R. Frosch, W. Hajdas, M. Janousch, P. R. Kettle, S. Ritt, Z. G. Zhao, Phys. Lett. **B361** (1995) 179-183; R. Bilger *et al.* [Karmen Collaboration], Phys. Lett. **B363** (1995) 41-45; P. Astier *et al.* [NOMAD Collaboration], Phys. Lett. **B527** (2002) 23-28.
- [11] R. Abela, M. Daum, G. H. Eaton, R. Frosch, B. Jost, P. R. Kettle and E. Steiner, Phys. Lett. B **105** (1981) 263 [Erratum-ibid. B **106** (1981) 513]; M. Daum, B. Jost, R. M. Marshall, R. C. Minehart, W. A. Stephens and K. O. H. Ziock, Phys. Rev. D **36** (1987) 2624; D. A. Bryman and T. Numao, Phys. Rev. D **53** (1996) 558.
- [12] M. Daum, M. Janousch, P. R. Kettle, J. Koglin, D. Pocanic, J. Schottmuller, C. Wigger, Z. G. Zhao, Phys. Rev. Lett. **85** (2000) 1815-1818.
- [13] Y. Asano, R. S. Hayano, E. Kikutani, S. Kurokawa, T. Miyachi, M. Miyajima, Y. Nagashima, T. Shinkawa *et al.*, Phys. Lett. **B104** (1981) 84; R. S. Hayano, T. Taniguchi, T. Yamanaka, T. Tanimori, R. Enomoto, A. Ishibashi, T. Ishikawa, S. Sato *et al.*, Phys. Rev. Lett. **49** (1982) 1305.
- [14] T. Yamazaki, in Proc. Neutrino'84 (Dortmund, 1984).
- [15] F. Bergsma *et al.* [CHARM Collaboration], Phys. Lett. **B128** (1983) 361; G. Bernardi, G. Carugno, J. Chauveau, F. Dicarolo, M. Dris, J. Dumarchez, M. Ferroluzzi, J. M. Levy *et al.*, Phys. Lett. **B166** (1986) 479; S. A. Baranov, Y. A. Batusov, A. A. Borisov, S. A. Bunyatov, V. Y. Valuev, A. S. Vovenko, V. N. Goryachev, M. M. Kirsanov *et al.*, Phys. Lett. **B302p** (1993) 336-340; A. Vaitaitis *et al.* [NuTeV and E815 Collaborations], Phys. Rev. Lett. **83** (1999) 4943-4946.
- [16] G. Bernardi, G. Carugno, J. Chauveau, F. Dicarolo, M. Dris, J. Dumarchez, M. Ferroluzzi, J. -M. Levy *et al.*, Phys. Lett. **B203** (1988) 332.

- [17] A. Kusenko, S. Pascoli, D. Semikoz, JHEP **0511** (2005) 028.
- [18] Y. Ashie *et al.* [Super-Kamiokande Collaboration], Phys. Rev. **D71** (2005) 112005.
- [19] P. Lipari, Astropart. Phys. **1** (1993) 195-227; P. Gondolo, G. Ingelman and M. Thunman, Astropart. Phys. **5** (1996) 309.
- [20] M. Honda, T. Kajita, K. Kasahara, S. Midorikawa, Phys. Rev. **D52** (1995) 4985-5005.
- [21] G. Battistoni, A. Ferrari, P. Lipari, T. Montaruli, P. R. Sala, T. Rancati, Astropart. Phys. **12** (2000) 315-333; M. Honda, T. Kajita, K. Kasahara, S. Midorikawa, Phys. Rev. **D70** (2004) 043008; M. Honda, T. Kajita, K. Kasahara, S. Midorikawa, T. Sanuki, Phys. Rev. **D75** (2007) 043006; M. Honda, T. Kajita, K. Kasahara, S. Midorikawa, Phys. Rev. **D83** (2011) 123001.
- [22] A. D. Dolgov, S. H. Hansen, G. Raffelt and D. V. Semikoz, Nucl. Phys. B **590** (2000) 562.
- [23] A. Atre, T. Han, S. Pascoli and B. Zhang, JHEP **0905** (2009) 030; T. Asaka, S. Eijima and H. Ishida, JHEP **1104** (2011) 011.
- [24] O. Ruchayskiy and A. Ivashko, arXiv:1112.3319 [hep-ph].
- [25] See for example, C. Ishihara, PhD Thesis, University of Tokyo, Feb. 2010, “Full three flavor oscillation analysis of atmospheric neutrino data observed in Super-Kamiokande”.
- [26] K. Abe, T. Abe, H. Aihara, Y. Fukuda, Y. Hayato, K. Huang, A. K. Ichikawa and M. Ikeda *et al.*, arXiv:1109.3262 [hep-ex].